Volume 7 | Number 2 | 14 January 2019 | Pages 191–450

Journal of Materials Chemistry C

Materials for optical, magnetic and electronic devices

rsc.li/materials-c

ISSN 2050-7526

ROYAL SOCIETY OF CHEMISTRY | Celebrating IYPT 2019

REVIEW ARTICLE

Johnny C. Ho *et al.*

Transparent metal-oxide nanowires and their applications in harsh electronics

Journal of
Materials Chemistry C

ROYAL SOCIETY OF CHEMISTRY

REVIEW

View Article Online
View Journal | View Issue

Cite this: J. Mater. Chem. C, 2019, 7, 202

Transparent metal-oxide nanowires and their applications in harsh electronics

Ziyao Zhou,[ab] Changyong Lan,[ac] Renjie Wei[ab] and Johnny C. Ho*[abd]

Due to their excellent physical and chemical properties, one-dimensional (1D) transparent metal-oxide nanostructures, especially nanowires (NWs), are widely considered to be promising candidates for next-generation high-performance electronics. Meanwhile, with increasing industrial demand for electronics which can reliably function in harsh environments, such as high humidity, high temperature, and robust operating environments, 1D metal-oxide nanostructures with wide bandgaps and high stabilities are attracting increasing interest for devices operating in extreme conditions. In this article, we provide a comprehensive review on the recent advances in high-performance transparent metal-oxide NWs and their corresponding device applications in harsh electronics. We begin with a brief introduction of different methodologies for the controllable synthesis of high-quality metal-oxide NWs, followed by an evaluation of the physical limitations of these nanomaterials and approaches for addressing their electrical contact issues. Importantly, the operating principles of transistors, photodetectors and gas sensors based on these 1D metal-oxide nanostructures as well as some excellent examples will be thoroughly discussed for harsh environment operation. The final section describes the challenges for the practical utilization of 1D metal-oxide nanostructures for industrial applications and concludes with an outlook on the future development of these NWs for harsh electronics.

Received 6th September 2018,
Accepted 25th October 2018

DOI: 10.1039/c8tc04501a

rsc.li/materials-c

Published on 07 November 2018. Downloaded on 1/12/2019 7:44:34 AM.

1. Introduction

Harsh electronics, a special type of electronics which are capable of operating at high humidity and in extreme environments, especially at high temperatures, have been in urgent demand by industry in recent years.[1–4] Traditionally, electronics that must function at high temperatures must rely on active or passive cooling systems; however, in some unique applications, cooling systems may not be available, such as utilization in

[a] Department of Materials Science and Engineering, City University of Hong Kong, Hong Kong SAR, China. E-mail: johnnyho@cityu.edu.hk
[b] Shenzhen Research Institute, City University of Hong Kong, Shenzhen 518057, China
[c] School of Optoelectronic Science and Engineering, University of Electronic Science and Technology of China, Chengdu 610054, China
[d] State Key Laboratory of Terahertz and Millimeter Waves, City University of Hong Kong, Hong Kong SAR, China

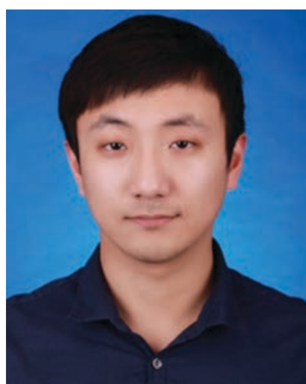

Ziyao Zhou

Ziyao Zhou received his BSc in Materials Physics in 2012 and his MSc in Materials Science and Engineering in 2015 from the Wuhan University (China). He is currently a PhD candidate at City University of Hong Kong (Hong Kong SAR). His research interests include the synthesis and characterization of wide bandgap semiconductor nanostructures and their applications in electronics and optoelectronics.

Changyong Lan

Changyong Lan received his BS degree in applied physics from the University of Electronic Science and Technology of China (UESTC) in 2007 and his PhD degree in physics from Nanjing University in 2012. Then, he joined UESTC as a lecturer. In 2016, he joined Johnny C. Ho's group at City University of Hong Kong as a post-doctoral researcher. His research interests are the controlled synthesis of low-dimensional functional materials and their applications in electronics and optoelectronics.

This journal is © The Royal Society of Chemistry 2019

Published on 07 November 2018. Downloaded on 1/12/2019 7:44:34 AM.

portable equipment. Also, high-end electronics which can operate at high temperatures to improve system reliability or decrease costs are appealing.[3] Generally, the physical properties of almost all semiconductor materials employed in electronics are heavily influenced by temperature. For example, the intrinsic carrier densities, carrier lifetimes, and leakage currents of semiconductors are all proportional to temperature. After these semiconductors are fabricated into electronic devices, some device parameters, such as carrier diffusion length, emitter efficiency, and base transport factors, are very sensitive to changes in temperature even if only slight fluctuation occurs.

Among many material properties, the major consideration of using semiconductors in a harsh environment (*e.g.* as hot as 300 °C) is the bandgap. Wide bandgap semiconductors, whose bandgaps are larger than 2 eV, offer exceptional advantages in terms of their high-power and high-frequency operations. To date, several types of wide bandgap semiconductors, including SiC, III-nitrides, and diamond, have been widely used as active channel materials for transistors and photodetectors operating under extreme conditions. However, there are still many deficiencies in the performance of these devices due to their unsuitable inherent physical properties. Specifically, the performance of electronic and photodetector devices based on Si are susceptible to temperature fluctuation and can degrade at elevated temperatures, with a large increase of the dark current. This unstable and unreliable performance severely restricts their practical utilization. Meanwhile, devices based on AlGaN or GaN are very sensitive to the ambient environment.[5] For example, AlGaN and GaN are easily oxidized to form metal oxides on their surfaces. These oxides act as shallow donor level defects, and the electrical and optical properties of AlGaN and GaN deteriorate gradually.[6] Notably, this degradation process is significantly accelerated at high temperatures. As a result, it is essential to integrate complicated packaging schemes of these AlGaN and GaN devices for practical deployment. Because of the associated high cost of these devices, no AlGaN and GaN-based harsh electronics are currently available in the commercial market.

At the same time, due to the advent of nanotechnology, one-dimensional (1D) metal-oxide nanostructures, such as nanowires (NWs), nanorods, nanotubes, and nanofibers, have stimulated great interest in the scientific community due to their extraordinary chemical and physical properties.[7] These 1D materials are considered to be ideal systems to explore a great number of novel phenomena at the nanoscale. In this regard, many efforts have been made to investigate the size and dimensionality dependence of the properties of these structures for various applications. In addition to evaluating their fundamental characteristics, these 1D metal-oxide nanostructures have also been used as active materials in fabricating electronic, optical, optoelectronic, electrochemical, and electromechanical devices, such as photodetectors,[8,9] single-electron transistors,[10] electron emitters,[11] field-effect transistors (FETs),[12–14] light-emitting diodes (LEDs),[15] biological and chemical sensors, and ultraviolet nanolasers.[16] More importantly, wide bandgap 1D metal-oxide nanostructures have excellent optical transparency in the visible region, high infrared reflectivity, and good electrical conductivity after doping.[17] In particular, In_2O_3 has a wide bandgap of 3.6 eV at room temperature. Recently, transistors built on As-doped In_2O_3 NWs integrated with an organic self-assembled nanodielectric layer as the dielectric layer exhibited an improved mobility as high as 2560 $cm^2\ V^{-1}\ s^{-1}$.[18] When fabricated into organic LED (OLED) devices, the optical transmittances before and after the OLED layer deposition were around 81% and 35% in the visible region, respectively. Due to this high conductivity and excellent transparency, In_2O_3 is now widely used in a rapidly increasing number of OLED industries. However, indium is rare in nature; thus, the material cost is

Renjie Wei

Renjie Wei received his BS and MS degrees from South-central University for Nationalities in 2011 and 2014, respectively. After that, he was employed as an assistant editor at MDPI. Currently, he is a PhD student under the supervision of Professor Johnny C. Ho in the Department of Materials Science and Engineering at City University of Hong Kong. His research interests are the fabrication of nanomaterials and their applications in electronics and energy conversion.

Johnny C. Ho

Johnny C. Ho received his BS with high honors in Chemical Engineering in 2002 and his MS and PhD in Materials Science and Engineering from the University of California, Berkeley, in 2005 and 2009, respectively. From 2009 to 2010, he worked as a post-doctoral research fellow in the nanoscale synthesis and characterization group at Lawrence Livermore National Laboratory, California. Currently, he is an Associate Professor of Materials Science and Engineering at City University of Hong Kong. His research interests focus on the synthesis, characterization, integration and device applications of nanoscale materials for various technological applications, including nanoelectronics, sensors and energy harvesting.

Published on 07 November 2018. Downloaded on 1/12/2019 7:44:34 AM.

relatively high. For this reason, cost-effective substitutes of indium are being extensively explored. Recently, SnO_2 has become attractive as an active material for low-cost transparent electronics instead of In_2O_3.[17,19,20] Due to its high optical transparency, relatively low cost compared with In_2O_3 and ease of forming ohmic-like contacts with electrodes, SnO_2 is currently being used to fabricate high-performance transistors, gas sensors, *etc.*[21–23]

Furthermore, due to their wide band-gaps (*e.g.* 3.7 eV for ZnO, 4.5 eV for Ga_2O_3, *etc.*), excellent stabilities at high temperature and ambient environment, low material cost and facile synthesis processes compared with other semiconductors, 1D metal-oxide NWs are anticipated to be competitive active material candidates for future harsh electronics, photodetectors and sensors.[24] These 1D metal-oxide nanostructures not only inherit the fascinating properties of their bulk forms, such as excellent piezoelectricity, chemical sensing, and photo-detection, but also possess unique properties associated with their highly anisotropic geometries and size confinement. Some specific properties that differ from the bulk include more complex electronic properties and crystal structures, a variety of oxidation states, coordination numbers, symmetries, crystal-field stabilization, stoichiometries, and acid–base surface properties; thus, these 1D NWs are suitable for various technological applications operating in extreme conditions.

In this article, we provide a comprehensive review of these high-performance transparent metal-oxide NWs as well as their utilization in harsh electronics, including transistors, photo-detectors, and gas sensors. We start with a brief introduction of the methodologies developed for the synthesis of these high-quality metal-oxide NWs. Different growth methods, such as vapor phase and solution-based methods, will be emphasized. Also, several useful examples of high-temperature stable electrodes will be discussed. These electrode developments are critical to address the electrical contact problem of harsh electronics, in which the contact issue is known to be one of the most significant critical factors for devices operating in extreme conditions. After that, metal-oxide–semiconductor FETs (MOSFETs), photo-detectors, and gas sensors based on different transparent metal-oxide NWs, predominantly ZnO, Ga_2O_3 and SnO_2, will be surveyed in detail.[20] Eventually, we will conclude this work with a discussion of certain perspectives and an outlook on the future applications of transparent 1D metal-oxide NWs for various types of harsh electronics under different operating environments.

2. Synthesis method

In general, various synthesis methods are employed to controllably produce 1D metal-oxide NWs. They can be briefly categorized into two major methods: (1) physical deposition and (2) chemical deposition. Typically, physical deposition methods include thermal evaporation, molecular beam epitaxy, confinement growth, sputtering, laser ablation, *etc.* Chemical deposition methods include chemical vapor deposition (CVD), hot-filament metal-oxide vapor deposition, thermal oxidation, and solvothermal and sol–gel syntheses. The main difference between these two types of synthesis techniques is that chemical deposition involves chemical reactions during the synthesis of 1D metal-oxide NWs, while physical deposition methods do not. In contrast, physical deposition methods are especially useful for controllable "top-down" growth processes, whereas chemical deposition methods are usually used in "bottom-up" growth processes. In any case, the purity and concentration of oxygen in the growth environment plays an important role in the synthesis of high-quality 1D metal-oxide NWs. For commercial and large-scale production considerations, chemical deposition methods are always preferred for the synthesis of 1D metal-oxide NWs because there are many more potential industrial manufacturing methods for practical applications.

2.1 CVD

In the semiconductor industry, various CVD techniques are employed for the fabrication of active device materials because of the superior controllability of the quality of the obtained materials compared to those achieved by physical vapor deposition methods. The conventional CVD techniques include metal–organic CVD, laser-ablation CVD, and plasma-enhanced CVD. Specifically, Fig. 1a shows a typical schematic of a tube furnace system employed for CVD synthesis.[25] Basically, all CVD methods are governed by two standard growth mechanisms, namely the vapor–liquid–solid (VLS) or vapor–solid–solid (VSS) mode and the vapor–solid (VS) mode.

VLS growth has been widely regarded as the fundamental synthesis mechanism for various types of 1D metal-oxide

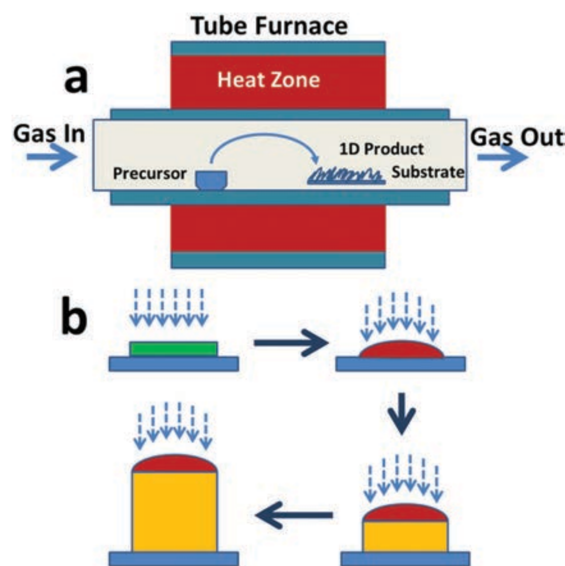

Fig. 1 (a) Schematic of a tube furnace for CVD synthesis of 1D nano-structures. (b) Schematics showing the typical vapor–liquid–solid (VLS) growth mechanism. The metallic nanoscale film (highlighted in green) is used as the catalytic seed which becomes the liquid eutectic alloy (highlighted in red) when heated to a specific temperature; then, reactive vapor (represented by dashed blue arrows) is continuously supplied. 1D nanostructures, such as NWs (highlighted in yellow), grow during the supersaturation of the catalytic seed.

This journal is © The Royal Society of Chemistry 2019

Published on 07 November 2018. Downloaded on 1/12/2019 7:44:34 AM.

nanostructures since it was reported for the growth of silicon whiskers in 1964.[26] Fig. 1b demonstrates a schematic of the VLS growth mechanism. Explicitly, the substrate is always deposited first with a metal film with dimensions on the nanometer scale. Later, during the growth, as the temperature increases, the metal film melts and yields metallic droplets that act as catalyst particles. With the continuous feeding of gaseous precursors, the metallic droplet and reactive precursor vapor next form a eutectic alloy in the liquid phase at a certain temperature. In other words, the reactive vapors act as the solutes dissolving into the metallic particles. As the dissolution continues, the liquid eutectic alloy gradually becomes saturated and then precipitates to form crystalline solid phases with specific growth orientations. In this case, 1D nanostructures can be grown by carefully maintaining the precursor supply and process temperature for an extended period of time. Because the entire process involves a precursor vapor, liquid eutectic alloy as the catalyst and a solid precipitate as the growth product, it is commonly referred to the VLS growth mode. Meanwhile, utilizing different kinds of catalyst metals and controlling the size of the metallic droplets are effective ways to reliably manipulate the sizes, shapes and surface morphologies of the obtained 1D nanostructures.[27,28] In some cases, when the catalytic alloy has an eutectic temperature higher than the NW growth temperature, a solid catalyst tip will form to yield the VSS growth mechanism shown here.[29–31]

In contrast, the main difference between the VS and VLS growth mechanisms is that catalytic particles are not required for the growth of 1D metal-oxide nanostructures *via* the VS growth mode.[32,33] Therefore, the VS mechanism is considered to be a self-catalytic process because only the precursor vapor and solid phase are involved in the growth process. In this scheme, the nanostructures usually grow along a preferential axis in which the crystal plane has the lowest energy and forms the 1D morphology. There are two main processes involved in the VS growth mechanism for the synthesis of 1D metal-oxide nanostructures: (1) The metal solid is first evaporated at high temperature to form the metal precursor vapor. Then, the metal vapor reacts with oxygen in the surrounding environment to yield the metal–oxygen vapor. For some metals with high boiling points, carbon powder is often required to function as a reducer to decrease the reaction temperature required to form the metal–oxygen vapor.[34] (2) Once the metal–oxygen vapor comes in contact with the substrate, it condenses into nanoscale droplets. Eventually, these small droplets grow into 1D crystalline nanostructures. Because no catalyst is involved in the growth process, the 1D crystalline nanostructures obtained *via* this VS mechanism are usually observed to have uncontrollable diameters or unfavorable morphologies (*e.g.* zig-zag patterns, nanocrystal chains and networks), abundant crystal defects on their surfaces, uneven radial NW growth, *etc.*[35–38] However, even though CVD techniques are highly regarded as competitive methods for low-cost and large-scale industrial production, several restrictions still remain; these include slow deposition rates, ease of chemical contamination, lack of ability to deposit multicomponent materials by precursors with different vaporization rates and temperatures simultaneously, high required deposition temperatures, difficulty of controlling the doping type and concentration, *etc.* It has been noted that the high deposition temperature of the CVD process can ensure good crystallinity and good thermal and chemical stability of the obtained 1D nanostructured semiconductors; however, at the same time, it limits their applications to integrated circuits because high temperatures can cause permanent damage to many properties of the underlying substrate. Furthermore, CVD-grown 1D nanostructured semiconductors always exhibit non-conventional intrinsic properties due to the uncontrollable growth process. For example, In_2O_3, SnO_2, and ZnO NWs grown by CVD normally show strong n-type conducting characteristics, which results from the intrinsic defects formed during the growth process.[38–40] Although p-type conduction was reported for ZnO NW arrays grown using P_2O_5 as a dopant, this p-type conduction was very unstable and readily changed to n-type conducting behavior after 2 months of storage in air.[41] Stable p-type doping of ZnO nanostructures is very difficult to obtain and has rarely been achieved in a reliable and controllable manner.

2.2 Hydrothermal method

Despite their advantages of producing highly crystalline metal-oxide NWs with excellent uniformity, the low throughput resulting from instrument limitation and high energy consumption associated with high reaction temperatures have restricted the use of CVD techniques for certain industrial applications, especially for those requiring highly efficient and low-cost manufacturing schemes. In this regard, solution-based production methods are anticipated to be one of the most competitive alternatives to CVD due to their unique advantages of high production yield, low energy cost and low instrument requirements.[42–44] Among many methods, hydrothermal and solvothermal schemes are the two most frequently used techniques. Compared with the hydrothermal method, the solvothermal method requires the use of organic solvents in both the reaction and subsequent cleaning processes if the reaction solvent is incompatible with water; thus, production is actually or potentially harmful to humankind and the environment.[45] On the other hand, the hydrothermal reaction takes place in an autoclave. Aqueous solutions of the reaction precursor and substrates are typically heated in an autoclave under temperatures of 100 °C to 300 °C and maintained for several hours or several days. More importantly, the obtained nanostructures can be effectively controlled by tuning the composition of the starting mixture precursors, reaction temperature and time, and pH value of the solvents as well as by using additional organic ligands and metal-ion impurities as auxiliary agents, using diverse solvents, *etc.* For example, as reported by Joo *et al.*, it is confirmed that pH-dependent electrostatic interactions between zinc reactants and the crystals can influence the preferential growth direction of ZnO NWs; this evidently suggests that these interactions provide a potential modality of control over the ZnO NW morphology.[46] The primary principle underlying this rational control during hydrothermal synthesis is face-selective electrostatic interaction. As illustrated in Fig. 2, by introducing ancillary non-zinc sulphates into this reaction,

Published on 07 November 2018. Downloaded on 1/12/2019 7:44:34 AM.

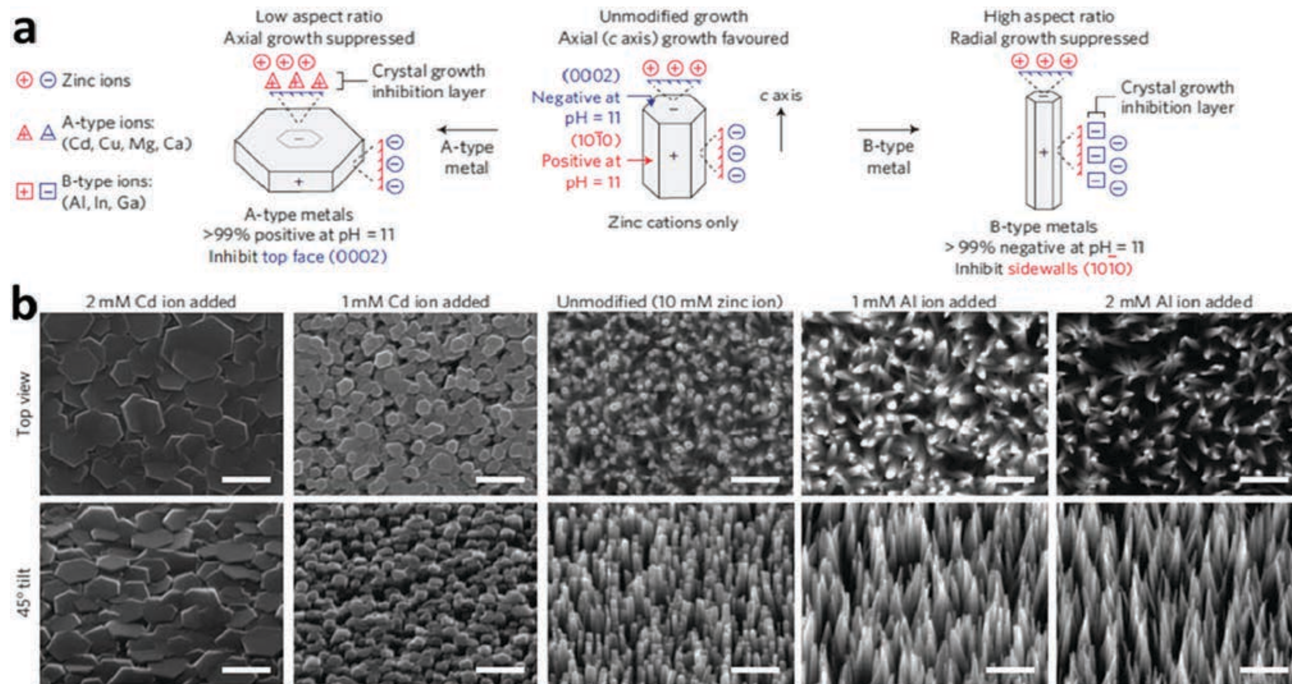

Fig. 2 (a) The morphology control mechanism of adding non-zinc metal sulphates to a bath solution during hydrothermal synthesis of metal-oxide nanostructures. A-type cations (positive at pH 11; Cd, Cu, Mg, and Ca) suppress axial growth at the negative (0002) face by limiting zinc complex-ion access, thus promoting platelet formation. Similar interactions between B-type ions (negative at pH 11; Al, In, Ga) and the positive (1010) sidewalls lead to high aspect ratio NWs. (b) Scanning electron microscope images of ZnO NWs grown in the presence of Cd or Al with different concentrations. Scale bars: 500 nm. Reproduced with permission from ref. 46. Copyright 2011, Springer Nature.

the local reaction environment during the growth can be systematically controlled. Ancillary metal sulphates that formed predominately positively charged complex ions at pH 11 were categorized as A-type (Cd, Cu, Mg, Ca), whereas ions that formed predominately negatively charged complexes were categorized as B-type (Al, In, Ga). The correlations between the aspect ratios of the NWs and the relative charge distributions of complex ions, in which A-type and B-type ions promoted low and high aspect ratio growth, respectively, were consistent for all the sulphates tested. Hence, the development of techniques for systematically manipulating the morphology of NWs synthesized by hydrothermal methods may further achieve the goal of electronics based on rational design of metal-oxide NW arrays.

3. Harsh electronics

For harsh electronics, various material factors of both their active and passive components can significantly limit their performance for operation in extreme conditions, especially at high temperatures.[47] Some physical properties and operating temperature limitations of selected materials and related devices

Table 1 Physical properties and operating temperatures of typical wide bandgap semiconductors and their corresponding devices

Semiconductor materials	Electron mobility ($cm^2 V^{-1} s^{-1}$)	Hole mobility ($cm^2 V^{-1} s^{-1}$)	Dielectric constant	Bandgap (eV)	Devices	Operating temperature (°C)	Ref.
4H-SiC	1000	50	—	3.26	JFET	300	48
					MOSFET	200	
6H-SiC	370	90	9.8	3.02	JFET	450	49
					MOSFET	500	50
					MESFET	250	51
Diamond	2200	1600	5.7	5.48	MESFETs	350	52
					Resistor	800	53
					JFET	250	54
GaN	1250	250	11	3.42	AlGaN/GaN HEMT	400	55
					FET	360	56
AlN	140	14	10	6.24	Photodetector	300	57
ZnO	3200	200	7.8	3.37	Photodetector	200	58
					RRAM	85	1
Ga_2O_3	880	—	9.9	4.9	Photodetector	427	59

This journal is © The Royal Society of Chemistry 2019

Published on 07 November 2018. Downloaded on 1/12/2019 7:44:34 AM.

are listed in Table 1, including junction FET (JFET), MOSFET, metal–semiconductor FET (MESFET), high-electron mobility transistors (HEMT) and resistive random access memory (RRAM). It is crucial to evaluate and understand these factors to further optimize material design and device structures. In this section, we will heavily focus on the assessment of the physical limits of electronics in high operating temperatures, followed by discussion of the use of wide bandgap metal-oxide NWs for specific applications in harsh environments.

3.1 General considerations

Generally, high temperature-induced performance degradation of semiconductor devices is observed in harsh electronics, in which the degradation arises from the intrinsic physical limitations of the device materials.[60] When the operating temperature increases to a specific point, the device can no longer function or fulfill the demands of the desired functionality of its circuitry.

3.1.1 Carrier concentration. The most important temperature-induced degradation mechanism is related to the concentration of free carriers, which governs the device operation. Insufficient control of the free carrier concentration is fatal for the operation of almost all semiconductor devices. Free carriers primarily arise from unintentional doping during material synthesis; the type of unintentional doping can determine the conduction type of a semiconductor. At room temperature, the electron concentration of a semiconductor mainly depends on the concentration of dopant in the semiconductor. If there is no dopant present, the semiconductor will still contain a certain number of thermal electron and hole carriers associated with the crystal at any given temperature.[60] This phenomenon is determined by the intrinsic properties of the semiconductor.[61] The concentration of these intrinsic carriers (n_i in cm^{-3}) exponentially depends on the temperature of the semiconductor, as follows:[62]

$$n_i = \sqrt{N_C N_V} e^{-E_G/2kT} \quad (1)$$

where T is the temperature (in Kelvin), k is the Boltzmann constant (8.62×10^{-5} eV K^{-1}), E_G is the energy bandgap of the semiconductor measured in electron volts (eV), and N_C and N_V are the effective conduction and valance band density of states of the semiconductor (cm^{-3}). E_G, N_C and N_V are fundamental material properties that have substantially less temperature dependence compared with the explicit temperature exponential ($-E_G/2kT$) term of eqn (1). In principle, wide bandgap semiconductors have bandgaps of around or above 3 eV, in which the intrinsic carrier concentrations are much lower than those of narrow bandgap semiconductors. Thus, wide bandgap semiconductors are usually more suitable for high temperature operation, even beyond 600 °C, due to their relatively lower intrinsic carrier concentrations (*e.g.* 400 °C for SiC p–n junction diodes, 500 °C for 6H-SiC MOSFET, 300 °C for 4H-SiC JFETs, and 1000 °C for diamond Schottky diodes).[63,64]

3.1.2 Leakage problems. In addition to the free carrier concentration, another common limitation is device leakage at high temperatures. When the carriers gain sufficient energy to overcome or tunnel through an energy barrier, they will be transported through the metal–semiconductor interface (*i.e.*, Schottky barrier contact). This process, called emission, increases with temperature as the carriers gain more thermal energy. The current resulting from carrier emission can be approximately expressed as a function of temperature and bias voltage in the following relationship:[62]

$$I \cong AK^*T^2 e^{-q\Phi_B/kT}(e^{qV_A/kT} - 1) \quad (2)$$

where Φ_B is the effective potential barrier height (*i.e.*, Schottky barrier height) of the junction and K^* is the effective Richardson constant of the semiconductor. For appreciable reverse biases ($V_A < -0.2$ V), the reverse-bias leakage current calculated from eqn (2) can be simplified to the following expression:

$$I \cong AK^*T^2 e^{-q\Phi_B/kT} \quad (3)$$

Eqn (3) clearly shows that the carrier emission current exponentially decreases with increasing effective potential barrier height. Although the barrier height strongly depends on the work function of the metal, the Fermi level of the semiconductor, and the junction formation process, in practice, the effective barrier heights of Schottky contacts based on most semiconductors and metals are usually less than three quarters of the semiconductor bandgap energy. Therefore, utilizing wide bandgap semiconductors in devices can lead to higher barrier heights and thus significantly decrease the junction leakage current at any given temperature by at least several orders of magnitude compared with that of narrow bandgap semiconductors. Meanwhile, for more practical applications, the use of a high work function metal can decrease the leakage current. By using Ni (5.1 eV work function) electrodes for capacitors, the leakage current at 125 °C can be decreased by nearly 2 orders of magnitude compared with that of devices using Al electrodes (4.1 eV work function).[65,66] All these intrinsic carrier and leakage limitations mainly impact the off-state currents of electronics at high operating temperatures; thus, their device components underperform in logic circuits, especially in transistors and random access memory arrays.

3.1.3 Carrier mobility. As the device operating temperature increases, the transport ability of carriers is accordingly suppressed because of the increased thermal vibrational energy of atoms in the crystal lattice. In other words, there are more collisions of carriers when the carriers move through the crystal in response to the electric field. This phenomenon is commonly known as phonon scattering; this mechanism decreases carrier mobility and subsequently decreases the amount of current that a diode or transistor can carry. In general, the acoustic phonon scattering probability increases with temperature and follows a $T^{3/2}$ power law behavior.[62] As another consequence, the carriers rapidly moving through the semiconductor are less deflected by ionized impurities at high temperatures or high electric fields because of the increased kinetic energy of the carriers. In this case, the ion impurity scattering probability changes with temperature following a $N_i T^{-3/2}$ law, where N_i is defined as the concentration of ionized impurities, mostly arising from the ionized dopants in semiconductors.[62] As specific examples,

Published on 07 November 2018. Downloaded on 1/12/2019 7:44:34 AM.

decreases in carrier mobility are observed for devices based on 4H-SiC, AlGaN/GaN junctions and GaN with increasing temperature. Consequently, the decreasing carrier mobility leads to a decrease of the current, which can degrade the fabricated integrated circuits of the devices.[67,68] All these examples clearly demonstrate the adverse effects of temperature changes on the carrier mobility of electronic devices.

3.1.4 Contacts. In addition to the above-discussed material properties, electrical contacts are also considered to be a vital factor for the performance of electronic devices at high temperatures.[69] In addition to the contacts designed for electronics functioning in an ordinary environment, the requirements for efficient electrical contacts for harsh electronics can be summarized as (1) low contact resistivity or good Schottky characteristics; (2) good adhesion; (3) high thermal stability; and (4) high environmental resistance. Conventional contacts are more prone to degradation at elevated temperatures, which is due to the fact that the semiconductor substrate and the metallization are not in thermodynamic equilibrium. High temperature usually has the following impacts on contact behavior: (1) increase of atomic mixing; (2) possible formation of new phases (solid-state reactions); (3) potential occurrence of oxidation; and (4) higher electromigration and thermomigration rates.[3] Typically, standard low work function metals, such as Ti, Cr and Al, are selected as contact electrode materials by considering their energy level matching and good adhesion to the substrate. However, these low work function metals are easily oxidized in ambient atmosphere and at high temperatures. In this regard, indium tin oxide (ITO) has been ubiquitous in practical thin-film electrode applications over the past several decades;[70,71] however, ITO is expensive due to the scarcity of indium element. Also, there are potential health issues associated with ITO due to exposure to indium-based powders.[72,73]

As reported by Zeng *et al.*, metal-oxide NWs-based sensors with excellent long-term durability can be achieved by introducing stable and low-resistance contacts on NWs using heavily doped metal oxides as contact materials (Fig. 3a).[74] Specifically, low-cost antimony-doped SnO_2 (ATO) contacts can enable electrical stability of SnO_2 NW sensors at 200 °C in air for at least 1960 hours, whereas conventional devices with Ti contacts exhibit significant electrical degradation in contact resistance (R_c) within several hours. As indicated by the *I–V* characteristics of the ATO-contacted device in Fig. 3b, the device maintains good linearity of curves, with only a slight increase in resistance. It should be noted that the ATO-contacted devices have high resistance immediately after ATO layer deposition. The electrical resistivity of the ATO film then greatly decreases by thermal annealing. In Fig. 3c, the variations of R_c are quite different between the Ti and ATO contacts. A rapid increase of R_c of the Ti contacts was clearly observed during a heating period of less than 200 h, while the R_c of the ATO contacts was almost constant over 1960 h. Fig. 3d and e also show the high temperature (200 °C) and long-term (186 hours) response values of both ATO and Ti-contacted gas sensors and photodetectors under 100 ppm NO_2 atmosphere and 260 nm ultra-violet (UV) light, respectively. The response of ATO-contacted devices was almost constant and

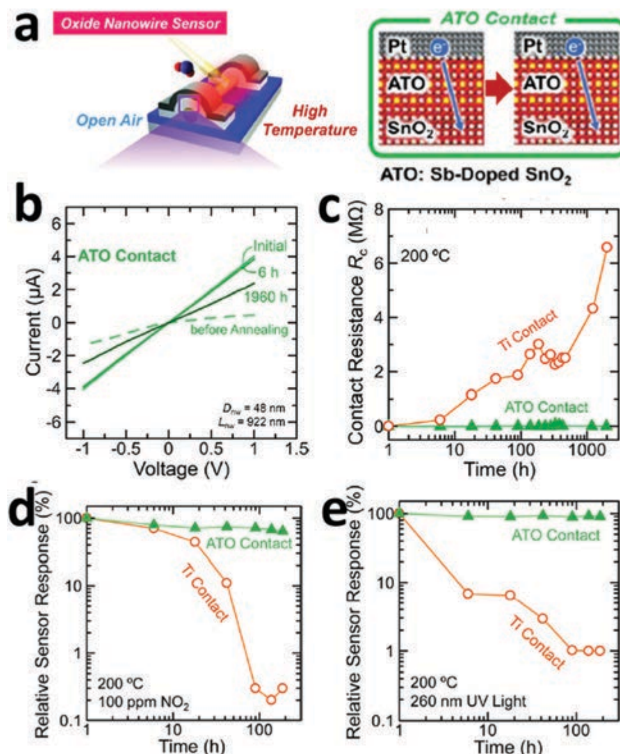

Fig. 3 (a) Design concept to achieve long-term stability and low resistance of electrical contacts on metal-oxide NWs. (b) *I–V* characteristics of heavily antimony-doped SnO_2 (ATO) contacts on SnO_2 NW devices in open air (initial and heated at 200 °C for 6 and 1960 hours, respectively). (c) Relationship between contact resistance (R_c) and duration of heating for devices with ATO contacts. (d) Relationship between relative sensing response to 100 ppm of N_2-balanced NO_2 and duration of heating (200 °C, open air). (e) Relationship between relative sensing response to UV light (260 nm) and duration of heating. The response values are normalized by the initial responses. Reproduced with permission from ref. 74. Copyright 2017, American Chemical Society.

did not degrade after more than 100 hours of measurements. The slight decrease in the response of the ATO-contacted device is presumably due to changes in the SnO_2 NW surface due to oxygen. The excellent characteristics of these low-cost ATO contacts were observed to lead to stable responses of fabricated gas sensors and photodetectors even after long-term heating and operation, which clearly indicates the practical advantages of these enhanced contacts for harsh electronics requiring long-term stability at high temperatures.

In addition to introducing heavily doped metal oxide contact layers, various novel electrode designs have also been carefully investigated for integration with devices operating in high temperature environments, such as carbon nanotubes and graphene, metal grids and metallic NW, *etc.*[75,76] However, carbon nanostructure-based materials cannot satisfy the requirements of transparency and conductivity, which are both essential for optoelectronic applications, such as solar cells and OLEDs. Metal nanogrids are less promising for large-scale and practical applications due to their high cost of their batch-based processing.[77] In comparison, metal-based (*e.g.* silver, Ag) NW networks have attracted much interest from researchers because

This journal is © The Royal Society of Chemistry 2019

Published on 07 November 2018. Downloaded on 1/12/2019 7:44:34 AM.

of their excellent electrical, mechanical, and optical properties as well as their processability in solution.[78,79] Meanwhile, due to the high speed, low-cost, roll-to-roll fabrication process of Ag NWs, they are competitive candidates for future electrode materials in industry.[80] They also show excellent transparence properties, which leads to their possible utilization in transparent electronics when combined with transparent wide bandgap oxide semiconductor active materials. In order to improve the thermal stability of Ag NW composite electrodes, polymers with higher glass transition temperatures, including polyimides and reinforced hybrid polymers, have been employed. A sandwich layer of zinc oxide (ZnO)/Ag NWs/ZnO was also investigated and confirmed to further increase the thermal stability of fabricated electrodes compared with freestanding Ag NWs.[81,82] Recently, as reported by Chen *et al.*, employing atomic layer deposition (ALD) at low temperature to coat a conformal and thin layer of ZnO around individual NWs can substantially enhance the thermal stability of Ag NWs while maintaining their porous structures.[83] TEM images of Ag NWs with and without ZnO are depicted in Fig. 4a to clearly illustrate that ZnO is completely wrapped around the Ag NW. Fig. 4b also shows the pristine Ag NWs heated at 250 °C after 30 min; they were found to completely convert into isolated droplets and fragmented NWs. Once coated with a 4.5 nm thick layer of ZnO, as shown in Fig. 4c, no further significant fragmentation or coalescence of the NWs was observed after heating even to a higher temperature of 300 °C for 30 min. In the case of the pure Ag NW film, a slight increase in the sheet resistance can be witnessed below 250 °C. When the temperature reaches a higher level, the sheet resistances begin to exhibit a dramatic increase (Fig. 4d). As expected, the ZnO enhanced electrode showed only a slight continuous increase in resistance as a function of temperature, without any rapid increase in resistance up to 500 °C. As a result, it is evident that the electrode based on ZnO-coated Ag NWs with high thermal stability is suitable for use in harsh electronics that require both high electrical and optical performance.

3.2 Harsh MOSFETs

In addition to contact issues, there are also many challenges to the development of device active materials for harsh electronics. Recently, β-Ga_2O_3, a thermally and chemically stable semiconductor material with a wide bandgap (approximately 4.9 eV), has attracted wide attention for transistors operating at high temperatures.[84] MESFETs, MOSFETs and Schottky barrier diodes based on bulk or epitaxially grown β-Ga_2O_3 crystals have been thoroughly investigated.[85] It can be anticipated that MOSFETs based on β-Ga_2O_3 nanostructures will also be inherently stable in the thermal sense and suitable to function as device materials for harsh electronics.

Particularly, as demonstrated by Kim *et al.*, MOSFETs based on exfoliated β-Ga_2O_3 nanobelts were successfully achieved, while their corresponding electrical characteristics were also systematically analyzed at elevated temperatures. The long-time stability of these devices was also carefully studied by storing them in ambient air for one month.[86] As shown in Fig. 5a, β-Ga_2O_3 nanobelts with a thickness of about 200 nm can be controllably separated from bulk β-Ga_2O_3 crystal by repeated application of the mechanical exfoliation technique with commercial Scotch tape. After the transfer, a back-gated transistor with Ti/Au (20 nm/80 nm) source/drain electrodes can be fabricated by standard photolithography, electron beam thin film evaporation and lift-off. Fig. 5b gives the typical output characteristics

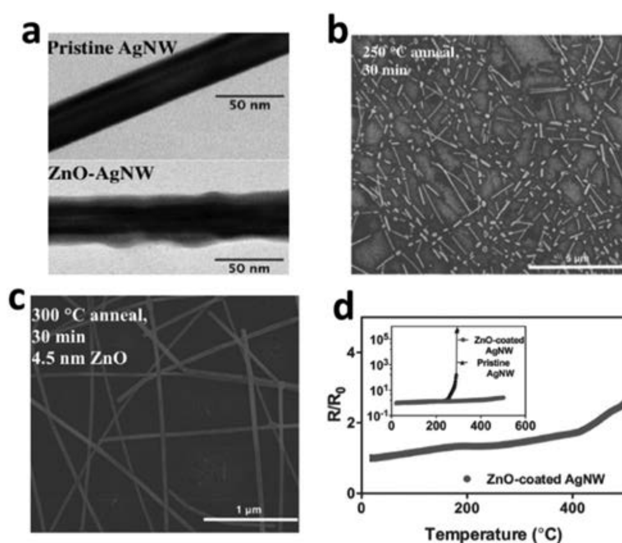

Fig. 4 (a) TEM images of pristine (top) and ZnO-coated Ag NWs (bottom). (b) SEM image of Ag NWs coated on a glass substrate after annealing at 250 °C for 30 min. (c) SEM image of 4.5 nm thick ZnO-coated Ag NWs after annealing at 300 °C for 30 min. (d) Normalized sheet resistance of a ZnO-coated Ag NW, with the normalized sheet resistance for the ZnO–Ag NW and pristine Ag NW plotted on a logarithmic scale in the inset. Reproduced with permission from ref. 83. Copyright 2015, John Wiley and Sons.

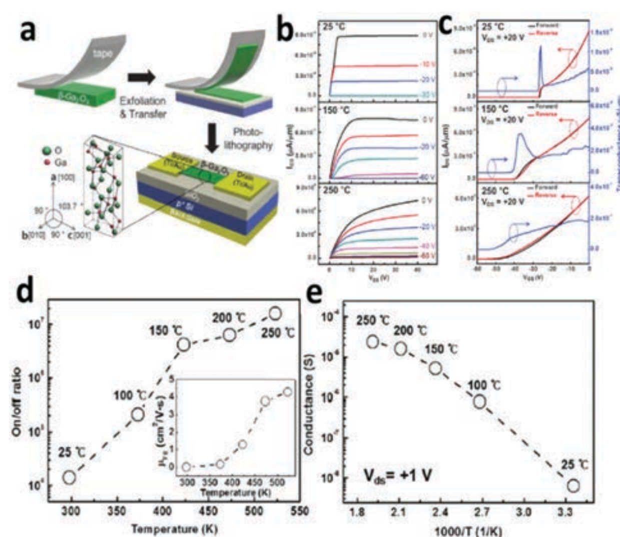

Fig. 5 (a) Exfoliation and transfer process of exfoliated β-Ga_2O_3 nanobelts to the target substrate and the related device structure. (b) I_{DS}–V_{DS} and (c) transfer characteristics at varying V_{GS} at temperatures ranging from 25 °C to 250 °C. Transistor (d) on/off ratios (inset: field-effect mobility) and (e) electrical conductance at temperatures ranging from 25 °C to 250 °C. Reproduced with permission from ref. 86. Copyright 1999, CCC Republication.

Published on 07 November 2018. Downloaded on 1/12/2019 7:44:34 AM.

(source–drain current *versus* source–drain voltage, I_{DS}–V_{DS}) of the β-Ga_2O_3 nanobelt MOSFETs at elevated operating temperatures. The n-type conductivity can be attributed to the oxygen vacancies and impurities that act as electron donors in the β-Ga_2O_3 nanostructures. Importantly, no electrical breakdown was observed in the measurements up to V_{DS} = +40 V and V_{GS} = 60 V between 25 °C and 250 °C, which indicates that devices fabricated with β-Ga_2O_3 nanobelts can maintain good performance at elevated temperatures. Fig. 5c illustrates the transfer characteristics (source–drain current *versus* source–gate voltage, I_{DS}–V_{GS}) of the fabricated β-Ga_2O_3 nanobelt FET at V_{DS} = +20 V and at 25 °C and 250 °C, respectively. It can be noted that the electrical properties, including transconductance and output currents, both improved with increasing operating temperature. The on/off current ratio, defined as the I_{DS} at V_{GS} = 0 V divided by the I_{DS} at V_{GS} = 60 V, was found to increase from approximately 10^4 to approximately 10^7 in the operating temperature range from 20 °C to 250 °C (Fig. 5d). As shown in Fig. 5e, the electrical conductance of the β-Ga_2O_3 nanobelts also increased with increasing temperature. At 25 °C, the field-effect mobility (μ_{FE}) was determined to be 1.5×10^{-3} cm^2 V^{-1} s^{-1}; however, it increased to 4.28 cm^2 V^{-1} s^{-1} when the temperature increased to 250 °C, which can be attributed to the increased transconductance at higher temperatures. All these results clearly indicate that β-Ga_2O_3 nanobelts are promising as the active materials for harsh electronics, especially for operation at high temperatures, compared with other wide bandgap semiconductor materials (*e.g.* GaN ∼ 3.4 eV and 4H-SiC ∼ 3.2 eV).[74] Meanwhile, the device performance can be further improved by controlling the free carrier concentrations by doping the shallow donors Sn and Si into the β-Ga_2O_3 lattice.

Compared with other electrical parameters, such as the on-current, carrier mobility, and sensing selectivity, of fabricated sensors, the capability of robust operation based on nanoscale transistors under harsh environments is also important.[87] For biomedical applications, in particular, transistor operation must be stable under diverse conditions, including ambient humidity and environments containing water, blood, and oxygen.[88] Many recent studies have demonstrated that device stability can be improved simply by using inorganic and/or organic passivation layers on the semiconductor surface. Impressively enhanced device stability with exposure to different ambient environments (*e.g.* bias stressing and light illumination) can be effectively achieved by this method. For example, inorganic SiO_x passivation can be utilized to improve the transconductance of FETs.[89] An organic self-assembled monolayer of 1-octadecanethiol was employed as a surface passivation layer to realize low-noise electronics based on NWs.[90] Moreover, an L-lysine surface passivation layer can be used to yield excellent stability against H_2O molecules, providing reproducible UV photoresponse in humid air and prohibiting the gradual degradation of the UV photocurrent of ZnO NWs.[91]

In detail, Lim *et al.* demonstrated the utilization of a self-assembled monolayer (SAM) of octadecylphosphonic acid (OD-PA) to passivate a functionalized NW transistor, allowing the device to operate consistently in various harsh operating environments.[92]

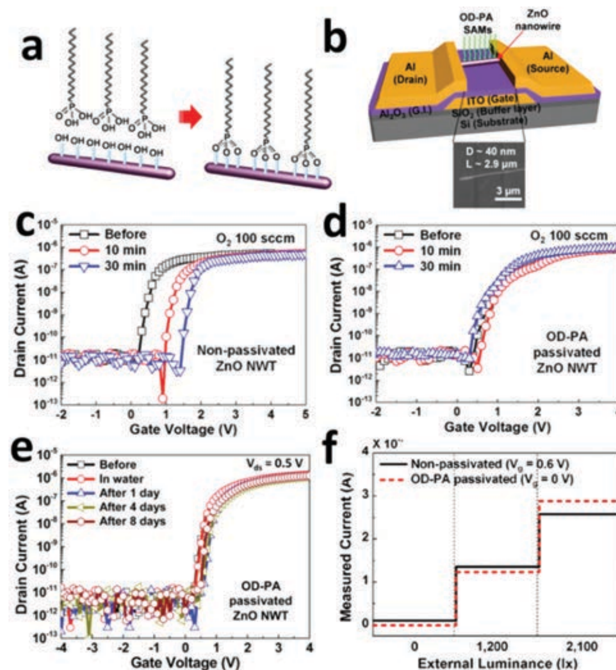

Fig. 6 Schematics of (a) OD-PA SAMs on ZnO NWs and (b) a bottom-gate-structured ZnO NW transistor (NWT). The inset shows a representative field-emission SEM image of the OD-PA-passivated NW-channel region between the source and drain electrodes. (c and d) Log-scale I_{DS}–V_{GS} characteristics of representative nonpassivated and OD-PA-passivated ZnO NWTs after exposure to oxygen. (e) OD-PA-passivated ZnO NWTs after exposure to water for 1 min. Measurements were performed over 8 days. (f) Two-step measured currents *via* external light intensities (dark, 1200 and 2100 lx). Reproduced with permission from ref. 92. Copyright 2015, American Chemical Society.

The surface of the ZnO NWs is first functionalized with a SAM of OD-PA. Strong chemical bonds are expected to form between the metal oxide surface and phosphonates *via* heterocondensation and metal–ligand coordination, as presented in Fig. 6a. A single passivated NW was then used in a bottom-gated ZnO device with ITO as the gate electrode, Al_2O_3 as the dielectric gate, and Al metal as the source/drain electrodes (Fig. 6b). Various conditions were then applied during the characterization of the fabricated NW transistor, including moisture, water, blood, oxygen, and light illumination. As shown in Fig. 6c and d, when exposed to representative oxygen conditions for different times, the log-scale I_{DS}–V_{GS} characteristics of the nonpassivated devices show dramatic changes in behavior with a bias of 0.5 V. In distinct contrast, the passivated devices show almost the same characteristics at different exposure times. Meanwhile, more measurements were taken to prove that the passivated ZnO NW transistors have excellent stability in response to exposure to other environments (*e.g.* water and blood). For example, once dipped in water, its I_{on} value would significantly decrease for the nonpassivated device and then gradually recover after 8 days. For the OD-PA-passivated ZnO NW transistors, the I_{on} value remained the same in water and exhibited stable electrical performance without any change for 8 days as shown in Fig. 6e. These results indicate that the OD-PA ZnO NW devices can maintain stable operating performance

This journal is © The Royal Society of Chemistry 2019

Published on 07 November 2018. Downloaded on 1/12/2019 7:44:34 AM.

over a long lifetime even in harsh external environments. As shown in Fig. 6f, when illuminated under different light densities (*e.g.* 0, 1200, and 2100 lx), the plots of I_{DS} for the both passivated and nonpassivated NW transistors showed the same step function with different current levels. The behavior was unchanged because the transmittance of an OD-PA self-assembled monolayer is 98% to 99% at wavelengths of 300 to 1200 nm and the monolayer of OD-PA does not decrease the transmittance of light. As a result, OD-PA-passivated ZnO NW transistors can be used as highly selective light sensors that are robust in humid conditions. All these findings demonstrate the capability of OD-PA passivation methods for fabricating commercial nanoelectronics operating in harsh environments without degrading their optical sensitivities.

3.3 Solar-blind harsh photodetectors

Recently, deep-ultraviolet (DUV) photodetectors functioning in the solar-blind spectrum range (*i.e.* 190 to 280 nm) have become a very popular scientific topic due to urgent requirements from industries, such as missile tracking, biomedicine and environmental monitoring.[93,94] Meanwhile, for many harsh environmental applications, including flame detection at high temperatures, DUV photodetectors capable of operating at elevated temperatures are also in great demand. Generally speaking, for the practical application of a photodetector, the 5S (*i.e.* high sensitivity, high signal-to-noise ratio, high spectral selectivity, high speed, and high stability) requirements must be satisfied.[95–97] Especially for high-temperature DUV detection, the 5S are even more important criteria than for room temperature operation.[98] Among many active materials, the electrical properties of traditional photodetector devices based on Si are very sensitive to temperature fluctuation.[99,100] Increasing temperature will lead to a proportional increase in the dark current and consequent degradation of these devices due to the inherent properties of the material, which limits their practical utilization. Thus, many wide bandgap semiconductor nanostructures, such as $ZnGa_2O_4$ NWs,[101] Zn_2GeO_4 NWs,[102] $Al_xGa_{1-x}N$,[103] $Mg_xZn_{1-x}O$,[104] ZnO,[105] and $In_2Ge_2O_7$ nanobelts,[106] have been thoroughly investigated for their capabilities as active sensing elements for DUV solar-blind photodetectors. With a bandgap of $\sim$4.9 eV, β-Ga_2O_3 is also an ideal candidate for visible-blind DUV-light sensors and optoelectronic circuits.[59] Recently, as developed by Zou *et al.*, β-Ga_2O_3 multi-layered nanobelts with (l00) facet-oriented can be readily synthesized and employed to fabricate photodetectors.[107] The as-fabricated photodetectors with β-Ga_2O_3 multi-layered nanobelts demonstrate excellent photosensing performance, that is, high sensitivity, high stability, high signal-to-noise ratio, high spectral selectivity, and fast time response. More importantly, all these performance parameters can be maintained at temperatures as high as 433 K. Fig. 7a shows the configuration of a photoconductive device based on facet-oriented β-Ga_2O_3 multi-layered nanobelts for photoresponse measurement. Fig. 7b presents the spectral response of the β-Ga_2O_3 nanobelt photodetector using a lock-in technique at a bias of 5 V at room temperature. It can be seen that the β-Ga_2O_3 nanobelt device is insensitive to light with wavelengths longer than 300 nm.

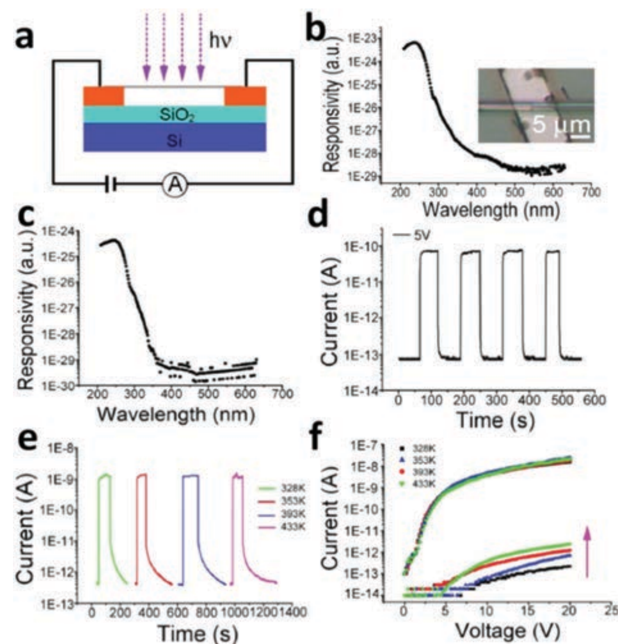

Fig. 7 (a) Schematic of a β-Ga_2O_3 nanobelt deep UV-light sensor configuration. (b) Spectroscopic photoresponse of a β-Ga_2O_3 nanobelt photodetector measured at a bias of 5 V under different wavelengths from 200 nm to 650 nm; the inset shows a SEM image of a β-Ga_2O_3 nanobelt device. (c) Spectroscopic photoresponse of the as-fabricated β-Ga_2O_3 nanobelt photodetector measured at 433 K under different wavelengths from 200 nm to 650 nm. (d) Time response of the β-Ga_2O_3 nanobelt photodetector illuminated by 250 nm light with an intensity of 9.835×10^{-5} W cm^{-2} at a bias of 5 V. (e) The ON/OFF cycle of the β-Ga_2O_3 nanobelt device upon 250 nm light illumination from room temperature to 433 K under the intensity of 9.835×10^{-5} W cm^{-2} at a bias of 6.0 V. (f) I–V characteristics of the as-fabricated β-Ga_2O_3 nanobelt device as the temperature changed from room temperature to 433 K. Reproduced with permission from ref. 107. Copyright 2014, John Wiley and Sons.

Meanwhile, Fig. 7c shows the spectral response of the device operated at a high temperature of 433 K. Similar to that at room temperature, the responsivity at 250 nm is also almost 6 orders of magnitude larger than that in the visible light range at 433 K. Furthermore, this value remains unchanged even at this high temperature, indicating that the device based on β-Ga_2O_3 nanobelts also possesses high-temperature selectivity towards solar-blind irradiation which is comparable to that at room temperature. As shown in Fig. 7d, the on- and off-state currents for each of the four cycles shown retain the same levels, illustrating the high reversibility and high stability of the β-Ga_2O_3 nanobelt optical switches over this time interval. The response time (t_r) and decay time (t_d) were observed to be shorter than 0.3 s. As depicted in Fig. 7e, when the temperature was increased to 433 K, the time response was thermally stable at elevated temperature and the current decreased by more than three orders of magnitude within 0.3 s. Fig. 7f also displays the I–V characteristics of the device with variation of temperature. At a fixed bias of 20 V, the photo-excited current remained constant as the temperature increased from 328 K to 433 K. The calculated photoresponsivity indicates thermal stability as the temperature increases. At the same time, there are two important performance parameters for photodetectors.

View Article Online

Published on 07 November 2018. Downloaded on 1/12/2019 7:44:34 AM.

One is the detector current responsivity (R_λ), which is defined as the photocurrent generated per unit power of the incident irradiation on the effective area of a photoconductor. The other is the external quantum efficiency (EQE), which is defined as the number of electrons detected per incident photon. It is impressive that the R_λ and EQE values of the β-Ga_2O_3 nanobelt high-temperature device were found to be 870, 970, 740, and 650 A W^{-1} and 4.3×10^3, 4.8×10^3, 3.6×10^3, and 3.2×10^3 as the temperature increased from 328, 353, and 393 to 433 K, respectively. The β-Ga_2O_3 nanobelt device exhibited high responsivity which is three orders of magnitude higher than those of other semiconductor photodetectors at high temperatures and even much better than those of the reported detectors at room temperature. All these results obviously imply that the (*l*00) facet-oriented β-Ga_2O_3 multi-layered nanobelts are promising candidates for harsh DUV photodetectors.

However, because of the large surface-to-volume ratios of the nanostructured materials, the present (*l*00) facet-oriented β-Ga_2O_3 multi-layered nanobelt photodetectors are still strongly affected by the high density of surface states for further performance enhancement.[107] Therefore, novel strategies are required to improve the stability of the photoresponse properties of β-Ga_2O_3 nanostructured photodetectors. Zou *et al.* reported a unique type of high-temperature and high-detectivity solar-blind DUV photodetector based on an individual β-Ga_2O_3 NW and found that the photoresponse behavior was dominated by the bulk rather than the surface states, largely due to the differences in the conducting channel geometry between the NWs and nanobelts.[108] They observed that the fabricated β-Ga_2O_3 NW photodetector shows fast response at elevated temperatures. The spectral response of the devices at a bias of 5 V measured at room temperature, 423 K, and 503 K exhibited different peak discrimination ratios in the range from 250 nm to 480 nm, which are 2×10^4 for room temperature, 10^4 for 423 K and 2×10^3 for 503 K. These temperature-dependent properties indicate good thermal stability of the β-Ga_2O_3 NW photodetector, and this high discrimination ratio would lead to the possibility of future applications in harsh photodetectors operating at high temperatures. Meanwhile, illuminated by 250 nm DUV light at 553 K with an intensity varying from 0.37 to 49 μW cm^{-2}, the *I–V* curves of the β-Ga_2O_3 NW photodetector showed similar photocurrent dependence behavior compared with that at room temperature. In order to clarify the independence of the photosensing properties from the surface state, measurements were taken under atmospheric pressure and vacuum pressures of 5 Pa and 250 Pa. As a consequence, the photocurrent at an applied voltage of 5 V increased only slightly from 4.6 to 5.1 nA when the vacuum level increased from atmospheric pressure to 5 Pa, while the response speed did not obviously decrease. The photocurrent of the β-Ga_2O_3 NW device mainly results from its two kinds of photo-generated carriers, which are generated from both the bulk and the surface. Because the photocurrent increases only slightly, bulk photo-generated carriers dominate the photoresponse behavior. The photocurrent under continuous increase of light density shows almost the same behavior in ambient and vacuum conditions. This also supports that the photocurrent transported within the β-Ga_2O_3 NW structure arises mainly from the bulk. From the above results, the bulk-dominated photoconductive β-Ga_2O_3 NW based device shows high sensitivity, high signal current-to-dark current, high spectral selectivity, high speed, high thermal stability, and insensitivity to vacuum conditions. Explicitly, all these properties completely meet the 5S requirements for a high-performance photodetector, which is in distinct contrast to the photodetector based on β-Ga_2O_3 nanobelts.

3.4 Gas sensors

In addition to photodetectors, 1D nanomaterials are competitive candidates for gas sensor applications due to their high surface-to-volume ratios and size effects. 1D semiconductors, including SnO_2,[109,110] ZnO,[111] WO_3,[112] and In_2O_3,[113] have been well investigated for their gas-sensing properties, such as sensitivity, fast response, and enhanced capability to detect low concentrations of gases compared with their corresponding thin films.[2,114] The sensing mechanism of these semiconducting metal oxides heavily relies on the surface conductivity induced by chemical reactions between the target gases and oxygen species adsorbed onto the surface. As shown in Fig. 8, for n-type semiconductors (*e.g.* SnO_2), oxygen molecules are adsorbed on the surface of the material and then combine with free electrons to form oxygen ions, consequently creating a depletion layer. When exposed to reducing gases (*e.g.* CO), the surface-bound oxygen ions are removed and the immobilized electrons are released, thereby decreasing the thickness of the depletion layer and leading to an increase in conductivity (*i.e.*, the resistance decreases).[115] In contrast, oxidizing gases (*e.g.* NO_2) further immobilize the electrons near the surface region by creating additionally charged surface-acceptor sites, which leads to increasing thickness of the depletion layer; subsequently, the conductivity decreases (*i.e.*, the resistance increases).[116–118] In contrast to other kinds of electronics, such as photodetectors, the characteristics of gas sensors benefit from their thermally activated electronic conductivities at elevated temperatures.[114] Thus, the demand for high-performance gas sensors for operation in harsh conditions necessitates a search for stability, sensitivity and a wide range of operating temperatures (from room temperature to high temperature).

Gas sensors fabricated from 1D nanomaterials usually show lower optimal operating temperatures, which is favorable for

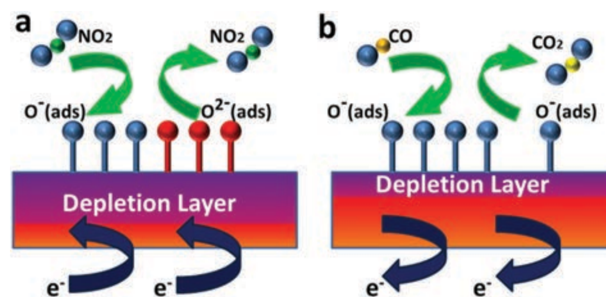

Fig. 8 Schematics of the gas sensing mechanisms of (a) oxidizing gases (NO_2) and (b) reducing gases (CO).

Published on 07 November 2018. Downloaded on 1/12/2019 7:44:34 AM.

power saving and device integration. Again, β-Ga_2O_3 is suitable to act as the active element for gas sensor applications at high temperatures.[119] Furthermore, this material is also thermodynamically stable in the entire operating temperature range up to its melting point (~1800 °C).[119,120] Meanwhile, it was proved that gallium oxide exhibits excellent sensibility to reducing gases, such as H_2, CO, and CH_x, on the basis of surface reactions below 700 °C. Above this temperature, gallium oxide can be used as an oxygen sensor based on the existence of oxygen vacancies.[121,122] Although this metal oxide is intrinsically an insulator, with a wide bandgap of 4.8 eV, it can still behave as an n-type semiconducting material at high temperatures; this conductivity results from defects induced during the synthesis process in a special atmosphere at high temperatures.[123] At elevated temperatures, the conductivity of β-Ga_2O_3 can also be influenced by ambient atmosphere. However, at low temperatures, the diffusion of oxygen vacancies is frozen and the bulk electrical conductivity no longer responds to changes in the composition of the surrounding gas. The high working temperature limits the application of β-Ga_2O_3-based gas sensors. Kim *et al.* developed a Pt-functionalized β-Ga_2O_3 NW gas sensor with a catalyst decorated on the surface to enhance its sensing properties for the detection of CO gas.[124] The bare β-Ga_2O_3 NWs showed responses of 4.2, 4.4, 5.0, and 6.6% at CO concentrations of 10, 25, 50, and 100 ppm, respectively. In contrast, the Pt-functionalized β-Ga_2O_3 NWs yield much improved responses of 115.4, 113.8, 110.9, and 111.7% at increasing CO concentrations, with enhancements of 27.8, 26.1, 22.0, and 16.9 fold, respectively. The long response time of 650 s and recovery time of 570 s of the Pt-functionalized β-Ga_2O_3 NW sensors remains a problem to be resolved because shorter response and recovery times are obviously desirable. The higher response of the Pt-functionalized β-Ga_2O_3 NW is mainly caused by the well-known spillover effect.[125–127] At high temperatures, reactive oxygen species, such as O^-, O^{2-}, and $O_2{}^-$, are chemosorbed onto the β-Ga_2O_3 NWs, which allows efficient electron transfer. On the other hand, this chemisorption and electron transfer rarely occur for bare β-Ga_2O_3 NWs at low temperatures. In the case of Pt-functionalized β-Ga_2O_3 NWs, the adsorption of reactive oxygen species is much easier due to the high conducting nature of Pt nanoparticles, which enables the chemisorption of reactive oxygen species on the material, even at low temperatures. As a result, enhanced sensing properties of the sensor to the target gases can be achieved at varied temperature conditions.

However, due to their earth-scarcity, the high cost of noble metals is an ongoing concern; therefore, reduction or complete elimination of noble metal usage in the catalysts and related catalytic sensors promises benefits not only for the relevant industries but also for global energy and environmental issues. Instead of Pt nanoparticle-decorated gas sensors for harsh environment operation, Lin *et al.* reported an alternative of $La_{0.8}Sr_{0.2}FeO_3$ (LSFO) nanoparticles, which can also dramatically sensitize metal oxide nanorod gas sensors at high temperatures.[128] Fig. 9a shows the gas sensing characteristics of the β-Ga_2O_3, β-Ga_2O_3/LSFO 5 nm, β-Ga_2O_3/LSFO 10 nm, and β-Ga_2O_3/Pt composite nanorods to varied CO gas concentrations (20, 50, 80, and 100 ppm in N_2 balance) at

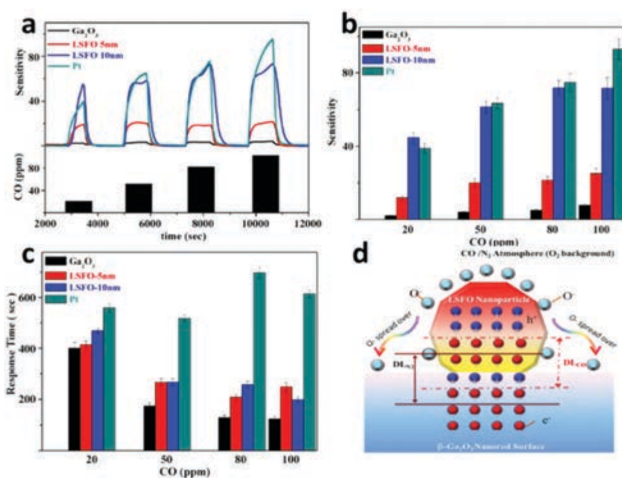

Fig. 9 (a) Current–time characteristics of β-Ga_2O_3, β-Ga_2O_3/LSFO 5 nm, β-Ga_2O_3/LSFO 10 nm, and β-Ga_2O_3/Pt composite nanorods tested at 500 °C with N_2 as the background atmosphere. (b) Sensitivity and (c) response time *versus* CO concentration characteristics of β-Ga_2O_3, β-Ga_2O_3/LSFO 5 nm, β-Ga_2O_3/LSFO 10 nm, and β-Ga_2O_3/Pt composite nanorods tested at 500 °C. (d) Spillover-like effect model in the LSFO nanoparticle-decorated β-Ga_2O_3 nanorod surface in CO/N_2 atmosphere; DL indicates the carrier depletion layer. Reproduced with permission from ref. 128. Copyright 2016, American Chemical Society.

500 °C with N_2 acting as the background atmosphere. All four devices demonstrate increasing CO sensitivity with increasing CO concentration. The pristine β-Ga_2O_3 nanorod arrays and 10 nm-LSFO-nanoparticle-decorated samples exhibit sensitivities of ~8 and ~70, respectively, at 100 ppm of CO and 500 °C. The enhanced sensing performance induced by LSFO approaches the performance of Pt nanoparticle-decorated β-Ga_2O_3 nanorods. In fact, at lower CO concentrations, the sensing performances of 10 nm LSFO and Pt nanoparticles are nearly identical (Fig. 9b). For all the examined CO concentrations, the LSFO-nanoparticle decoration has a shorter response time than the Pt-nanoparticle decoration while having comparable or slightly longer response times compared with the pristine β-Ga_2O_3 nanorods (Fig. 9c). The high performance of the LSFO nanoparticle-decorated β-Ga_2O_3 nanorod gas sensors can be attributed to a spillover-like effect on their surfaces in CO/N_2 atmosphere.[129–131] Due to their exhibited p-type semiconductor characteristics, the LSFO nanoparticles can form p–n junctions with n-type β-Ga_2O_3 NWs on the surface. As shown in Fig. 9d, due to its surface-dominant nature, it is possible that the built-in-potential of p–n junctions will regulate the electrons and holes involved in the surface conduction upon gas exposure. The gas–LSFO–β-Ga_2O_3 triple-interface may function as a sink that attracts surface oxygen species, such as O^-, from the surface of the LSFO nanoparticles, which leads it to spread over to the β-Ga_2O_3 nanorod surface. Meanwhile, the insensitive response of the LSFO film to CO exposure indicates slow or negligible reactions between O^- and CO on the LSFO surface, which enables the formation of a concentration gradient driving the spread of oxygen ions on the less-consumed LSFO surface toward the LSFO/β-Ga_2O_3 interfaces and β-Ga_2O_3 nanorod surfaces. At low temperatures, the gas sensing mechanism

Published on 07 November 2018. Downloaded on 1/12/2019 7:44:34 AM.

towards target gases is dominated by the surface adsorption/desorption process. Therefore, the perovskite-type material-induced spillover-like effect can enhance the gas sensing performance of β-Ga_2O_3 nanorods at low temperatures. On the other hand, the resulting populated oxygen dissociation events and subsequently generated surface oxygen species on the LSFO nanoparticle surfaces may contribute to the shorter response times of LSFO–Ga_2O_3 nanorod sensors compared to Pt-decorated sensors. The demonstrated perovskite LSFO-nanoparticle-modified Ga_2O_3 nanorods are less expensive and show competitive performance; thus, they can serve as promising candidates for high-end sensor materials for high-temperature gas detection.

At the same time, some flammable gases in specific conditions of nature can also lead to enormous hazards. One important example is methane, which is a colorless and odorless flammable gas that is a main constituent of natural gas. Methane gas is highly volatile and readily explodes when mixed with air in a specific concentration range due to its high flammability. Thus, the development of a reliable and cost-effective methane gas sensor remains a substantial challenge for the timely detection of its conspicuous presence in our environment. However, in contrast to O_2 and CO sensors, a sensitive gas sensor for methane is difficult to achieve because methane molecules have high chemical stability and low activation energies, which make them very difficult to react with semiconductors.[132] Significant efforts have been made to detect methane at various temperature conditions using material systems, including single-walled and multi-walled carbon nanotubes loaded with palladium (Pd), as well as a Batron phosphorus–silicon microsensor. Among these, 1D metal-oxide nanostructured materials are considered to be one of the most promising candidates for future methane gas sensors due to their wide range of operating temperatures and high durability. As demonstrated by Biaggi-Labiosa *et al.*, a methane sensor based on porous SnO_2 nanorods has been developed.[132] The sensor has a wide operating temperature range (25 °C to 500 °C) for CH_4 detection (2500 to 125 ppm). They found that the porous SnO_2 nanorod sensor showed an obvious response to 0.25% CH_4 at room temperature. The same device also clearly responded to the gas as the temperature continuously increased to 500 °C with the baseline maintained at a reasonably stable level. Among all measured operating temperatures, 300 °C was the optimized operating temperature for CH_4 detection at all concentrations. In contrast to other gas sensors, in this study, the resistance even increased at the higher temperature of 500 °C. The mechanism of this observed behavior is currently under study; one possible explanation is that at high temperatures, in metal oxide semiconductors such as SnO_2, the mobility of oxygen vacancies becomes appreciable and the mechanism of conduction becomes mixed ionic–electronic conduction. This is a highly undesirable result that leads to mobile donors and produces slow and irreversible changes in the resistance of these sensors. After approximately 190 h of testing, the SnO_2 nanorod sensor exhibited improved response to the gas at room temperature, and the baseline remained at almost the same value. It was also noted that the porous SnO_2 nanorods are more sensitive than non-porous SnO_2 nanorods, nanobelts or nanocrystalline thin films because gas molecules can freely pass in and out of the porous nanorods through the pores and interact with the outer as well as the inner surfaces of the nanorods. The results shown here evidently indicate the uniqueness of these porous SnO_2 nanorods as an active sensing element that can effectively detect CH_4 from room temperature up to 500 °C. As a result, the porous SnO_2 sensor can be operated in harsh environments as a methane gas sensor.

4. Conclusion and outlook

In summary, this article provides a comprehensive review of the recent advances in 1D metal-oxide nanostructures for electronics, photodetectors, and gas sensors dedicated to operation in harsh environments. Meanwhile, we also discussed the physical limitations of the abovementioned devices functioning at high temperatures or under other robust operating conditions, followed by the introduction of several strategies to overcome these limitations. While metal-oxide NWs-based harsh electronics have been studied for decades and some encouraging progress has been achieved in this field, there is still much room for further exploration. We believe that there are substantial problems that still must be addressed for the practical utilization of metal-oxide NWs for harsh electronics and other applications.

First, the fabrication of harsh electronics is mainly based on high-quality single crystalline metal-oxide NWs. Although many synthesis techniques are already employed to produce high-quality metal-oxide NWs that have proved to be promising active material candidates for future industrial applications, the yield of these NWs still cannot satisfy the demand for scalable device fabrication and integration. Compared to vapor phase methods, hydrothermal methods have higher material production yields; however, the quality of the products is relatively low due to the fact that more defects are introduced during the synthesis process, which is critical for device performance.

Second, researchers have made great efforts to achieve the synthesis of NWs with controllable shapes, sizes, and compositions. However, the excellent controllability of the shapes, size, and compositions of NWs cannot guarantee the same controllability of their chemical or physical properties. The electrical properties, especially the threshold voltage, of metal-oxide NW based transistors are still unmanageable. For the catalyst-assisted vapor phase method, the diameters of the NWs strongly depend on the size of the catalyst droplets, which is determined by the random melting process of the starting noble metal nanoscale thin films or the uniformity of the metal colloids. Therefore, the electrical parameters of different devices always vary in a wide range, limiting their practical utilization in integrated circuits. Predictably, the nonstoichiometry of the metal-oxide NWs will lead to the same problem.

Third, to fabricate harsh electronics based on NWs, photolithography-based fabrication processes are commonly employed as device fabrication techniques. In the developing and removing processes of photolithography, various types of organic solvents are used. Consequently, organic groups are introduced and

 This journal is © The Royal Society of Chemistry 2019

Published on 07 November 2018. Downloaded on 1/12/2019 7:44:34 AM.

reside on the surfaces of the NWs, forming a high number of surface states; this can strongly affect the performance of harsh electronics, especially photodetectors and gas sensors, in which the surface states play an important role in their operation. A low-cost, practical, and simple method for fabrication of harsh electronics that consumes less organic solvent is highly desired.

Fourth, the working principle of metal-oxide NW-based gas sensors usually depends strongly on their absorption and desorption reactions. Therefore, these devices are very sensitive to the surrounding gas atmosphere, and their sensitivity even increases as the operating temperature increases. In this case, it is necessary to package the devices with low-cost materials and simple processes in order to prevent undesired reactions between metal-oxide NWs and the surrounding atmosphere. The practical utilization of these metal-oxide NW-based harsh electronics urgently requires the development of associated device packaging technologies.

In any case, 1D nanostructure-based harsh electronics show excellent potential for practical applications, such as combustion systems, well logging, industrial processes, vehicle brakes, nuclear reactors, and dense electronic packages. With the rapid development of nanomaterial synthesis and packaging techniques, it can be foreseen that commercial applications of 1D nanostructure-based harsh electronics in industry will be realized in the near future.

Conflicts of interest

There are no conflicts to declare.

Acknowledgements

We acknowledge the General Research Fund (CityU 11213115) of the Research Grants Council of Hong Kong SAR, China, the National Natural Science Foundation of China (Grants 51672229 and 61605024), the Science Technology and Innovation Committee of Shenzhen Municipality (Grant JCYJ 20170818095520778) and a grant from the Shenzhen Research Institute, City University of Hong Kong, and Fundamental Research Funds for the Central Universities (ZYGX2018J056).

Notes and references

1 P.-K. Yang, C.-H. Ho, D.-H. Lien, J. R. Durán Retamal, C.-F. Kang, K.-M. Chen, T.-H. Huang, Y.-C. Yu, C.-I. Wu and J.-H. He, *Sci. Rep.*, 2015, **5**, 15087.
2 R. Moos, N. Izu, F. Rettig, S. Reiß, W. Shin and I. Matsubara, *Sensors*, 2011, **11**, 3439–3465.
3 M. R. Werner and W. R. Fahrner, *IEEE Trans. Ind. Electron.*, 2001, **48**, 249–257.
4 T.-H. Huang, P.-K. Yang, D.-H. Lien, C.-F. Kang, M.-L. Tsai, Y.-L. Chueh and J.-H. He, *Sci. Rep.*, 2014, **4**, 4402.
5 B. C. Chung and M. Gershenzon, *J. Appl. Phys.*, 1992, **72**, 651–659.
6 G. A. Slack, L. J. Schowalter, D. Morelli and J. A. Freitas Jr, *J. Cryst. Growth*, 2002, **246**, 287–298.
7 R. S. Devan, R. A. Patil, J. H. Lin and Y. R. Ma, *Adv. Funct. Mater.*, 2012, **22**, 3326–3370.
8 N. Liu, G. Fang, W. Zeng, H. Zhou, F. Cheng, Q. Zheng, L. Yuan, X. Zou and X. Zhao, *ACS Appl. Mater. Interfaces*, 2010, **2**, 1973–1979.
9 J. D. Prades, R. Jimenez-Diaz, F. Hernandez-Ramirez, L. Fernandez-Romero, T. Andreu, A. Cirera, A. Romano-Rodriguez, A. Cornet, J. R. Morante, S. Barth and S. Mathur, *J. Phys. Chem. C*, 2008, **112**, 14639–14644.
10 A. Fujiwara, H. Inokawa, K. Yamazaki, H. Namatsu, Y. Takahashi, N. M. Zimmerman and S. B. Martin, *Appl. Phys. Lett.*, 2006, **88**, 053121.
11 B. Ling, X. W. Sun, J. L. Zhao, C. Ke, S. T. Tan, R. Chen, H. D. Sun and Z. L. Dong, *J. Phys. Chem. C*, 2010, **114**, 18390–18395.
12 Y. W. Heo, L. C. Tien, Y. Kwon, D. P. Norton, S. J. Pearton, B. S. Kang and F. Ren, *Appl. Phys. Lett.*, 2004, **85**, 2274–2276.
13 P. Nguyen, H. T. Ng, T. Yamada, M. K. Smith, J. Li, J. Han and M. Meyyappan, *Nano Lett.*, 2004, **4**, 651–657.
14 W. I. Park, J. S. Kim, G. C. Yi and H. J. Lee, *Adv. Mater.*, 2005, **17**, 1393–1397.
15 R. Könenkamp, R. C. Word and M. Godinez, *Nano Lett.*, 2005, **5**, 2005–2008.
16 H. Yan, R. He, J. Johnson, M. Law, R. J. Saykally and P. Yang, *J. Am. Chem. Soc.*, 2003, **125**, 4728–4729.
17 T. Minami, *Semicond. Sci. Technol.*, 2005, **20**, S35.
18 P.-C. Chen, G. Shen, H. Chen, Y.-g. Ha, C. Wu, S. Sukcharoenchoke, Y. Fu, J. Liu, A. Facchetti and T. J. Marks, *ACS Nano*, 2009, **3**, 3383–3390.
19 H. Hosono, *Thin Solid Films*, 2007, **515**, 6000–6014.
20 Ç. Kılıç and A. Zunger, *Phys. Rev. Lett.*, 2002, **88**, 095501.
21 C.-L. Hsu and Y.-C. Lu, *Nanoscale*, 2012, **4**, 5710–5717.
22 J. H. Yu and G. M. Choi, *Sens. Actuators, B*, 2001, **75**, 56–61.
23 V. V. Sysoev, T. Schneider, J. Goschnick, I. Kiselev, W. Habicht, H. Hahn, E. Strelcov and A. Kolmakov, *Sens. Actuators, B*, 2009, **139**, 699–703.
24 P. D. C. King and T. D. Veal, *J. Phys.: Condens. Matter*, 2011, **23**, 334214.
25 Z. W. Pan, Z. R. Dai and Z. L. Wang, *Science*, 2001, **291**, 1947.
26 R. S. Wagner and W. C. Ellis, *Appl. Phys. Lett.*, 1964, **4**, 89–90.
27 B. Wang, Y. Yang, N. Xu and G. Yang, *Phys. Rev. B: Condens. Matter Mater. Phys.*, 2006, **74**, 235305.
28 Y. Yan, L. Zhou, J. Zhang, H. Zeng, Y. Zhang and L. Zhang, *J. Phys. Chem. C*, 2008, **112**, 10412–10417.
29 H. Han, Y. Wang, Z. Yang, S. P. Yip, Z. Wang, D. Li, T. F. Hung, F. Y. Wang, Y. Chen and J. C. Ho, *J. Mater. Chem. C*, 2017, **5**, 4393–4399.
30 Z. Yang, L. Liu, S. P. Yip, D. Li, L. Shen, Z. Zhou, N. Han, T. F. Hung, E. Y. B. Pun, X. Wu, A. Song and J. C. Ho, *ACS Nano*, 2017, **11**, 4237–4246.
31 N. Han, F. Y. Wang, A. T. Hui, J. J. Hou, G. C. Shan, X. Fei, T. F. Hung and J. C. Ho, *Nanotechnology*, 2011, **22**, 285607.
32 A. Umar, S. Kim, Y.-S. Lee, K. Nahm and Y. Hahn, *J. Cryst. Growth*, 2005, **282**, 131–136.

View Article Online

Published on 07 November 2018. Downloaded on 1/12/2019 7:44:34 AM.

33 Y.-R. Ma, C.-M. Lin, C.-L. Yeh and R.-T. Huang, *J. Vac. Sci. Technol., B: Microelectron. Nanometer Struct.–Process., Meas., Phenom.*, 2005, **23**, 2141–2145.
34 J. Zhang, X. Qing, F. Jiang and Z. Dai, *Chem. Phys. Lett.*, 2003, **371**, 311–316.
35 J. Lao, J. Huang, D. Wang and Z. Ren, *Adv. Mater.*, 2004, **16**, 65–69.
36 Y. Yan, Y. Zhang, H. Zeng, J. Zhang, X. Cao and L. Zhang, *Nanotechnology*, 2007, **18**, 175601.
37 K. C. Kam, F. Deepak, A. Cheetham and C. Rao, *Chem. Phys. Lett.*, 2004, **397**, 329–334.
38 D. Chen, Z. Liu, B. Liang, X. Wang and G. Shen, *Nanoscale*, 2012, **4**, 3001–3012.
39 C. H. Park, S. B. Zhang and S.-H. Wei, *Phys. Rev. B: Condens. Matter Mater. Phys.*, 2002, **66**, 073202.
40 X. Li, Y. Yan, T. A. Gessert, C. L. Perkins, D. Young, C. DeHart, M. Young and T. J. Coutts, *J. Vac. Sci. Technol., A*, 2003, **21**, 1342–1346.
41 B. Xiang, P. Wang, X. Zhang, S. A. Dayeh, D. P. R. Aplin, C. Soci, D. Yu and D. Wang, *Nano Lett.*, 2007, **7**, 323–328.
42 S. H. Ko, D. Lee, H. W. Kang, K. H. Nam, J. Y. Yeo, S. J. Hong, C. P. Grigoropoulos and H. J. Sung, *Nano Lett.*, 2011, **11**, 666–671.
43 B. Liu and H. C. Zeng, *J. Am. Chem. Soc.*, 2003, **125**, 4430–4431.
44 X. Wang and Y. Li, *J. Am. Chem. Soc.*, 2002, **124**, 2880–2881.
45 H. G. Choi, Y. H. Jung and D. K. Kim, *J. Am. Ceram. Soc.*, 2005, **88**, 1684–1686.
46 J. Joo, B. Y. Chow, M. Prakash, E. S. Boyden and J. M. Jacobson, *Nat. Mater.*, 2011, **10**, 596.
47 P. L. Dreike, D. M. Fleetwood, D. B. King, D. C. Sprauer and T. E. Zipperian, *IEEE Trans. Compon., Packag., Manuf. Technol.*, 1994, **17**, 594–609.
48 W. Yi, C. Callaway, T. Ke, N. Harsh, T. P. Chow, D. Boroyevich and F. Wang, Proc. IEEE Power Electron. Specialists Conf., 2008.
49 A. C. Patil, X. Fu, C. Anupongongarch, M. Mehregany and S. Garverick, Proc. IEEE Compound Semicond. Integr. Circuit Symp., 2007.
50 N. S. Rebello, F. S. Shoucair and J. W. Palmour, *IEEE Proc. Circuits Dev. Syst.*, 1996, **143**, 115–122.
51 J. B. Casady, E. D. Luckowski, R. W. Johnson, J. Crofton and J. R. Williams, Proc. IEEE Electron. Comp. Tech. Conf., 1995.
52 A. Vescan, P. Gluche, W. Ebert and E. Kohn, *IEEE Electron Device Lett.*, 1997, **18**, 222–224.
53 A. Aleksov, M. Kubovic, N. Kaeb, U. Spitzberg, A. Bergmaier, G. Dollinger, T. Bauer, M. Schreck, B. Stritzker and E. Kohn, *Diamond Relat. Mater.*, 2003, **12**, 391–398.
54 V. K. Dmitriev, V. N. Inkin, G. G. Kirpilenko, B. G. Potapov, E. A. Ilyichev and E. Y. Shelukhin, *Diamond Relat. Mater.*, 2001, **10**, 1007–1010.
55 Y. Cai, Y. Zhou, K. M. Lau and K. J. Chen, *IEEE Trans. Electron Devices*, 2006, **53**, 2207–2215.
56 S. Binari, *Proc. - Electrochem. Soc.*, 1995, **95**, 21.
57 D.-S. Tsai, W.-C. Lien, D.-H. Lien, K.-M. Chen, M.-L. Tsai, D. G. Senesky, Y.-C. Yu, A. P. Pisano and J.-H. He, *Sci. Rep.*, 2013, **3**, 2628.
58 W. Lien, D. Tsai, S. Chiu, D. G. Senesky, R. Maboudian, A. P. Pisano and J. He, *IEEE Electron Device Lett.*, 2011, **32**, 1564–1566.
59 T. Wei, D. Tsai, P. Ravadgar, J. Ke, M. Tsai, D. Lien, C. Huang, R. Horng and J. He, *IEEE J. Sel. Top. Quantum Electron.*, 2014, **20**, 112–117.
60 W. Wondrak, *Microelectron. Reliab.*, 1999, **39**, 1113–1120.
61 P. G. Neudeck, R. S. Okojie and L.-Y. Chen, *Proc. IEEE*, 2002, **90**, 1065–1076.
62 S. M. Sze and K. K. Ng, *Physics of semiconductor devices*, John Wiley & Sons, 2006.
63 M. Willander, M. Friesel, Q.-u. Wahab and B. Straumal, *J. Mater. Sci.: Mater. Electron.*, 2006, **17**, 1.
64 J. B. Casady and R. W. Johnson, *Solid-State Electron.*, 1996, **39**, 1409–1422.
65 K. C. Chiang, C. C. Huang, H. C. Pan, C. N. Hsiao, J. W. Lin, I. J. Hsieh, C. H. Cheng, C. P. Chou, A. Chin, H. L. Hwang and S. P. McAlister, *J. Electrochem. Soc.*, 2007, **154**, G54–G57.
66 K. C. Chiang, C. H. Cheng, H. C. Pan, C. N. Hsiao, C. P. Chou, A. Chin and H. L. Hwang, *IEEE Electron Device Lett.*, 2007, **28**, 235–237.
67 W. Wondrak, R. Held, E. Niemann and U. Schmid, *IEEE Tran. Ind. Electron.*, 2001, **48**, 307–308.
68 S. Arulkumaran, T. Egawa, H. Ishikawa and T. Jimbo, *Appl. Phys. Lett.*, 2002, **80**, 2186–2188.
69 R. I. Rodriguez, D. Ibitayo and P. O. Quintero, *IEEE Trans. Compon., Packag., Manuf. Technol.*, 2013, **3**, 549–557.
70 B. Zhang, X. Dong, X. Xu, X. Wang and J. Wu, *Mater. Sci. Semicond. Process.*, 2007, **10**, 264–269.
71 O. J. Gregory, Q. Luo and E. E. Crisman, *Thin Solid Films*, 2002, **406**, 286–293.
72 T. Hamaguchi, K. Omae, A. Tanaka, M. Hirata, T. Takebayashi, Y. Kikuchi, N. Yoshioka, Y. Nishiwaki, O. Taguchi and T. Chonan, *Occup. Environ. Med.*, 2008, **65**, 51–55.
73 Q. Wan, E. N. Dattoli, W. Y. Fung, W. Guo, Y. Chen, X. Pan and W. Lu, *Nano Lett.*, 2006, **6**, 2909–2915.
74 H. Zeng, T. Takahashi, M. Kanai, G. Zhang, Y. He, K. Nagashima and T. Yanagida, *ACS Sens.*, 2017, **2**, 1854–1859.
75 M. W. Rowell, M. A. Topinka, M. D. McGehee, H.-J. Prall, G. Dennler, N. S. Sariciftci, L. Hu and G. Gruner, *Appl. Phys. Lett.*, 2006, **88**, 233506.
76 K. S. Kim, Y. Zhao, H. Jang, S. Y. Lee, J. M. Kim, K. S. Kim, J.-H. Ahn, P. Kim, J.-Y. Choi and B. H. Hong, *Nature*, 2009, **457**, 706.
77 J. Zou, H.-L. Yip, S. K. Hau and A. K.-Y. Jen, *Appl. Phys. Lett.*, 2010, **96**, 96.
78 J. Li, J. Liang, X. Jian, W. Hu, J. Li and Q. Pei, *Macromol. Mater. Eng.*, 2014, **299**, 1403–1409.
79 Y. Ahn, Y. Jeong and Y. Lee, *ACS Appl. Mater. Interfaces*, 2012, **4**, 6410–6414.
80 M. Singh, T. R. Rana, S. Kim, K. Kim, J. H. Yun and J. Kim, *ACS Appl. Mater. Interfaces*, 2016, **8**, 12764–12771.
81 Q. Huang, W. Shen, X. Fang, G. Chen, Y. Yang, J. Huang, R. Tan and W. Song, *ACS Appl. Mater. Interfaces*, 2015, **7**, 4299–4305.
82 A. Kim, Y. Won, K. Woo, C.-H. Kim and J. Moon, *ACS Nano*, 2013, **7**, 1081–1091.

This journal is © The Royal Society of Chemistry 2019

Published on 07 November 2018. Downloaded on 1/12/2019 7:44:34 AM.

83 D. Chen, J. Liang, C. Liu, G. Saldanha, F. Zhao, K. Tong, J. Liu and Q. Pei, *Adv. Funct. Mater.*, 2015, **25**, 7512–7520.

84 M. Higashiwaki, K. Sasaki, A. Kuramata, T. Masui and S. Yamakoshi, *Phys. Status Solidi A*, 2013, **211**, 21–26.

85 M. Bartic, *Phys. Status Solidi A*, 2016, **213**, 457–462.

86 J. Kim, S. Oh, M. A. Mastro and J. Kim, *Phys. Chem. Chem. Phys.*, 2016, **18**, 15760–15764.

87 B. Nasr, D. Wang, R. Kruk, H. Rösner, H. Hahn and S. Dasgupta, *Adv. Funct. Mater.*, 2013, **23**, 1750–1758.

88 Y. Zhang, K. Yu, D. Jiang, Z. Zhu, H. Geng and L. Luo, *Appl. Surf. Sci.*, 2005, **242**, 212–217.

89 Y. Cui, Z. Zhong, D. Wang, W. U. Wang and C. M. Lieber, *Nano Lett.*, 2003, **3**, 149–152.

90 S. Kim, P. D. Carpenter, R. K. Jean, H. Chen, C. Zhou, S. Ju and D. B. Janes, *ACS Nano*, 2012, **6**, 7352–7361.

91 L. Jinzhang, P. Jaeku, P. Kyung Ho, A. Yeonghwan, P. Ji-Yong, K. Ken Ha and L. Soonil, *Nanotechnology*, 2010, **21**, 485504.

92 T. Lim, J. Bong, E. M. Mills, S. Kim and S. Ju, *ACS Appl. Mater. Interfaces*, 2015, **7**, 16296–16302.

93 E. Monroy, F. Omnès and F. Calle, *Semicond. Sci. Technol.*, 2003, **18**, R33.

94 A. Soltani, H. A. Barkad, M. Mattalah, B. Benbakhti, J. C. De Jaeger, Y. M. Chong, Y. S. Zou, W. J. Zhang, S. T. Lee, A. BenMoussa, B. Giordanengo and J. F. Hochedez, *Appl. Phys. Lett.*, 2008, **92**, 053501.

95 L. Sang, J. Hu, R. Zou, Y. Koide and M. Liao, *Sci. Rep.*, 2013, **3**, 2368.

96 L. Hu, M. M. Brewster, X. Xu, C. Tang, S. Gradečak and X. Fang, *Nano Lett.*, 2013, **13**, 1941–1947.

97 X. Li, C. Gao, H. Duan, B. Lu, Y. Wang, L. Chen, Z. Zhang, X. Pan and E. Xie, *Small*, 2012, **9**, 2005–2011.

98 T. Zhai, X. Fang, M. Liao, X. Xu, H. Zeng, B. Yoshio and D. Golberg, *Sensors*, 2009, **9**, 6504–6529.

99 B. Joonho, K. Hyunjin, Z. Xiao-Mei, H. D. Cuong, Z. Yue, C. Young Jin, N. Arto and W. Zhong Lin, *Nanotechnology*, 2010, **21**, 095502.

100 A. Zhang, S. You, C. Soci, Y. Liu, D. Wang and Y.-H. Lo, *Appl. Phys. Lett.*, 2008, **93**, 121110.

101 P. Feng, J. Y. Zhang, Q. Wan and T. H. Wang, *J. Appl. Phys.*, 2007, **102**, 074309.

102 C. Li, Y. Bando, M. Liao, Y. Koide and D. Golberg, *Appl. Phys. Lett.*, 2010, **97**, 161102.

103 C. J. Collins, U. Chowdhury, M. M. Wong, B. Yang, A. L. Beck, R. D. Dupuis and J. C. Campbell, *Appl. Phys. Lett.*, 2002, **80**, 3754–3756.

104 T. Tsuyoshi, T. Hiroshi, F. Shizuo and F. Shigeo, *J. Appl. Phys.*, 2003, **42**, L401.

105 D.-S. Tsai, C.-A. Lin, W.-C. Lien, H.-C. Chang, Y.-L. Wang and J.-H. He, *ACS Nano*, 2011, **5**, 7748–7753.

106 L. Li, P. S. Lee, C. Yan, T. Zhai, X. Fang, M. Liao, Y. Koide, Y. Bando and D. Golberg, *Adv. Mater.*, 2010, **22**, 5145–5149.

107 R. Zou, Z. Zhang, Q. Liu, J. Hu, L. Sang, M. Liao and W. Zhang, *Small*, 2014, **10**, 1848–1856.

108 R. Zou, Z. Zhang, J. Hu, L. Sang, Y. Koide and M. Liao, *Nanotechnology*, 2013, **24**, 495701.

109 A. Kolmakov, Y. Zhang, G. Cheng and M. Moskovits, *Adv. Mater.*, 2003, **15**, 997–1000.

110 E. Comini, G. Faglia, G. Sberveglieri, Z. Pan and Z. L. Wang, *Appl. Phys. Lett.*, 2002, **81**, 1869–1871.

111 Q. Wan, Q. H. Li, Y. J. Chen, T. H. Wang, X. L. He, J. P. Li and C. L. Lin, *Appl. Phys. Lett.*, 2004, **84**, 3654–3656.

112 A. Ponzoni, E. Comini, G. Sberveglieri, J. Zhou, S. Z. Deng, N. S. Xu, Y. Ding and Z. L. Wang, *Appl. Phys. Lett.*, 2006, **88**, 203101.

113 D. Zhang, Z. Liu, C. Li, T. Tang, X. Liu, S. Han, B. Lei and C. Zhou, *Nano Lett.*, 2004, **4**, 1919–1924.

114 H. Steinebach, S. Kannan, L. Rieth and F. Solzbacher, *Sens. Actuators, B*, 2010, **151**, 162–168.

115 N. Bârsan and U. Weimar, *J. Phys.: Condens. Matter*, 2003, **15**, R813.

116 S. Das and V. Jayaraman, *Prog. Mater. Sci.*, 2014, **66**, 112–255.

117 A. Kolmakov and M. Moskovits, *Annu. Rev. Mater. Res.*, 2004, **34**, 151–180.

118 S. Park, S. An, Y. Mun and C. Lee, *ACS Appl. Mater. Interfaces*, 2013, **5**, 4285–4292.

119 Z. Liu, T. Yamazaki, Y. Shen, T. Kikuta, N. Nakatani and Y. Li, *Sens. Actuators, B*, 2008, **129**, 666–670.

120 M. Bartic, C.-I. Baban, H. Suzuki, M. Ogita and M. Isai, *J. Am. Ceram. Soc.*, 2007, **90**, 2879–2884.

121 T. Schwebel, M. Fleischer, H. Meixner and C. D. Kohl, *Sens. Actuators, B*, 1998, **49**, 46–51.

122 M. Fleischer, J. Giber and H. Meixner, *Appl. Phys. A: Mater. Sci. Process.*, 1992, **54**, 560–566.

123 Z. Li, C. d. Groot and J. H. Moodera, *Appl. Phys. Lett.*, 2000, **77**, 3630–3632.

124 H. Kim, C. Jin, S. An and C. Lee, *Ceram. Int.*, 2012, **38**, 3563–3567.

125 N. Yamazoe, *Sens. Actuators, B*, 1991, **5**, 7–19.

126 M. Schweizer-Berberich, J. G. Zheng, U. Weimar, W. Göpel, N. Bârsan, E. Pentia and A. Tomescu, *Sens. Actuators, B*, 1996, **31**, 71–75.

127 M. Hübner, D. Koziej, J.-D. Grunwaldt, U. Weimar and N. Barsan, *Phys. Chem. Chem. Phys.*, 2012, **14**, 13249–13254.

128 H.-J. Lin, J. P. Baltrus, H. Gao, Y. Ding, C.-Y. Nam, P. Ohodnicki and P.-X. Gao, *ACS Appl. Mater. Interfaces*, 2016, **8**, 8880–8887.

129 A. Kolmakov, D. O. Klenov, Y. Lilach, S. Stemmer and M. Moskovits, *Nano Lett.*, 2005, **5**, 667–673.

130 H. Hongtao, T. Shouqin, X. Jing, X. Zhong, Z. Dawen, C. Di and S. Guozhen, *Nanotechnology*, 2012, **23**, 105502.

131 N. Barsan and U. Weimar, *J. Electroceram.*, 2001, **7**, 143–167.

132 A. Biaggi-Labiosa, F. Sola, M. Lebrón-Colón, L. Evans, J. Xu, G. Hunter, G. Berger and J. Gonzalez, *Nanotechnology*, 2012, **23**, 455501.